ACS Catalysis

Research Article

pubs.acs.org/acscatalysis

Pt Nanoclusters Confined within Metal–Organic Framework Cavities for Chemoselective Cinnamaldehyde Hydrogenation

Zhiyong Guo,[†,‡,§] Chaoxian Xiao,[†,‡,§] Raghu V. Maligal-Ganesh,[†,‡] Lin Zhou,[‡] Tian Wei Goh,[†,‡] Xinle Li,[†,‡] Daniel Tesfagaber,[†,‡] Andrew Thiel,[†] and Wenyu Huang*[,†,‡]

[†]Department of Chemistry, Iowa State University, Ames, Iowa 50011, United States

[‡]Ames Laboratory, USDOE, Ames, Iowa 50011, United States

Supporting Information

ABSTRACT: A highly selective and robust catalyst based on Pt nanoclusters (NCs) confined inside the cavities of an amino-functionalized Zr-terephthalate metal–organic framework (MOF), UiO-66-NH_2 was developed. The Pt NCs are monodisperse and confined in the cavities of UiO-66-NH_2 even at 10.7 wt % Pt loading. This confinement was further confirmed by comparing the catalytic performance of Pt NCs confined inside and supported on the external surface of the MOF in the hydrogenation of ethylene, 1-hexene, and 1,3-cyclooctadiene. The benefit of confining Pt NCs inside UiO-66-NH_2 was also demonstrated by evaluating their performance in the chemoselective hydrogenation of cinnamaldehyde. We found that both high selectivity to cinnamyl alcohol and high conversion of cinnamaldehyde can be achieved using the MOF-confined Pt nanocluster catalyst, while we could not achieve high cinnamyl alcohol selectivity on Pt NCs supported on the external surface of the MOF. The catalyst can be recycled ten times without any loss in its activity and selectivity. To confirm the stability of the recycled catalysts, we conducted kinetic studies for the first 20 h of reaction during four recycle runs on the catalyst. Both the conversion and selectivity are almost overlapping for the four runs, which indicates the catalyst is very stable under the employed reaction conditions.

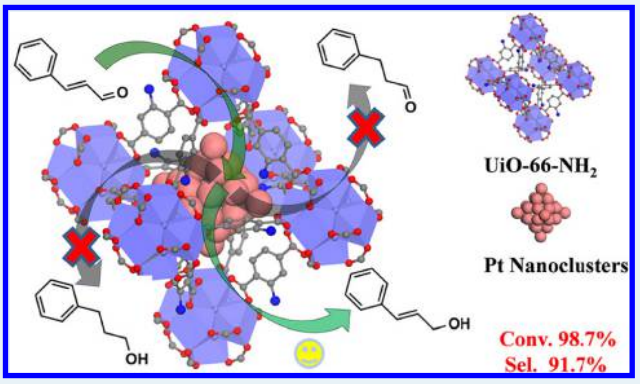

KEYWORDS: *metal–organic frameworks, nanoclusters, heterogeneous catalysis, chemoselectivity, cinnamaldehyde hydrogenation*

1. INTRODUCTION

Supported metal catalysts are one of the most important classes of heterogeneous catalysts. The active phase, often a transition metal, is dispersed over a support to maximize its surface area and prevent sintering during high-temperature reactions. Minimizing the usage of transition metals, especially precious metals, has been a major research direction in catalyst discovery and optimization. Nanoparticles (NPs) have been a major research focus in heterogeneous catalysis due to their high surface to volume ratio, and thus large surface areas exposed to reactants. Further reduction of the size of metal particles to the nanocluster level (diameter <2 nm) in catalysis is even more attractive because metal nanoclusters (NCs) composed of fewer than 100 atoms exhibit novel properties that differ greatly from those predicted by simple scaling laws.[1,2] Pd NCs of precisely controlled sizes (Pd_n, for n = 1, 2, 4, 7, 10, 16, 20, and 25) that were deposited on rutile TiO_2 (110) showed a strong size effect on their catalytic activity in CO oxidation.[3] The activity of these Pd NCs of different sizes was found to correlate exactly with the position of their X-ray photoelectron spectroscopy (XPS) peaks, which indicates that the valence electronic structure of these NCs controls their catalytic activity. We seek to synthesize confined monodisperse metal NCs inside the cavities of metal–organic frameworks (MOFs) to achieve desired catalytic properties.

MOFs have attracted tremendous research interest and a wide spectrum of applications have been demonstrated in gas storage and separation, carbon dioxide capture, guest dependent luminescence, and catalysis.[4−11] Heterogeneous catalysis using MOF-supported small metal NPs or NCs has attracted increasing research attention because the nanopores of MOFs can not only serve as templates for synthesizing monodisperse metal NPs/NCs but also provide well-defined microenvironments that could induce selectivity control on the encapsulated NPs/NCs in catalytic reactions. The loading of metal NPs/NCs into MOFs was first realized by chemical vapor deposition using volatile organometallic precursors in the gas phase.[12,13] More recently, by loading metal precursors in solution, Ag, Au, Ni, Pd, Ru, or Pt NPs and NCs of 1.4−10 nm in diameter have been prepared in various MOFs.[14−23] However, it is extremely

Received: October 26, 2013
Revised: March 17, 2014
Published: March 22, 2014

   dx.doi.org/10.1021/cs400982n | ACS Catal. 2014, 4, 1340−1348

difficult to achieve complete encapsulation of NPs/NCs inside MOFs.[24−26] Fully encapsulating NPs/NCs inside the cavities of MOFs is critical for making monodisperse metal NPs/NCs and demonstrating the benefit of using MOFs as the catalyst support. Typically, the NPs/NCs formed on MOFs have a broad size distribution and a substantial number of particles are larger than the diameter of the channels or the cavities inside the MOFs. These large metal particles are most likely supported on the external surface of the MOFs and do not fully experience the microenvironments provided by the cavities of MOFs, which complicates the catalyst system and makes it difficult to study the origin of enhanced activity or selectivity on catalysts based on MOF-supported NPs/NCs.

There are only few reports that show limited success in entrapping metal NPs/NCs inside the cavities of MOFs. Using chemical vapor deposition, Fischer and co-workers demonstrated that Au NCs that were confined in the cavities of ZIF-90 (1.2−1.3 nm) could be synthesized at a loading of 30 wt %.[24] However, many particles with diameters larger than 2 nm are still present in the sample. Kim and co-workers successfully prepared Ni NPs embedded inside a mesoporous MOF (MesoMOF-1) using gas-phase loading and subsequent reduction.[27] Unfortunately, TEM images did not show any obvious NPs. Using the wetness impregnation method, Latroche group used MIL-100(Al) as a host to synthesize Pd nanoparticles (most of them around 2.0 nm) embedded within the pores of the MOF.[28] Recently, Xu and co-workers synthesized Pt NPs and NCs inside the pores of MIL-101 without observing any aggregation of Pt particles on the external surfaces of the framework by using a "double solvents" method.[25] Nevertheless, the formed Pt particles have a size distribution of 1.2−3 nm in diameter, and the loading of the Pt is also relatively low (5 wt %). Here we used a MOF with small cavities, UiO-66-NH_2, as the scaffold and synthesized NCs that were confined in their cavities.

UiO-66 is built up from $[Zr_6O_4(OH)_4(CO_2)_{12}]$ clusters linked with 1,4-benzenedicarboxylic acid.[29] It leads to an overall porous cubic architecture. The framework itself comprises tetrahedral and octahedral cages, in a 2:1 ratio, of free dimensions close to 7.5 and 12 Å, respectively. Access to the cages is provided by narrow triangular windows with a free diameter close to 6 Å. UiO-66 and its amino functionalized isostructure UiO-66-NH_2 show great potential for many applications due to their good thermal stability, resistance toward atmospheric moisture, and large accessible pore volume. The large pore volume of UiO-66-NH_2 is appropriate for the loading of metal precursors. Moreover, the amine groups on terephthalic acid linkers in UiO-66-NH_2 could provide coordination sites for metal ions.

Using UiO-66-NH_2 as the template and support, we synthesized Pt NCs confined inside its cavities. The Pt NCs are monodisperse and confined in the cavities of the MOF even at 10.7 wt % Pt loading. After confirming that these Pt NCs are confined inside the cavities of the MOF, we tested their performance in the hydrogenation of cinnamaldehyde. We found that both high chemoselectivity to cinnamyl alcohol and high conversion of cinnamaldehyde can be achieved using the MOF-confined Pt nanocluster catalyst. The catalyst has been recycled ten times without any loss in its activity and selectivity.

2. EXPERIMENTAL SECTION

2.1. Materials and Synthesis. *Synthesis of UiO-66 and UiO-66-NH_2.* UiO-66 and UiO-66-NH_2 were synthesized using the reported procedure.[29] All syntheses of the Zr-based metal−organic frameworks were performed in 480 mL Teflon PFA wide mouth jars. $ZrCl_4$ (0.48 g, 2.058 mmol; 98%, Acros Organics) was dissolved in 120 mL of *N*,*N*′-dimethylformamide (DMF; ACS grade, Macron) by using sonication for about 5 min. The linker was added to the clear solution in an equimolar ratio with regard to $ZrCl_4$ (0.342 g, 2.058 mmol terephthalic acid (98%, Sigma-Aldrich) for UiO-66; 0.372 g, 2.058 mmol 2-aminoterephthalic acid (>99%, Sigma-Aldrich) for UiO-66-NH_2) and dissolved by sonication for about 5 min. When preparing UiO-66-NH_2, water (0.15 mL, 8.232 mmol) was added to the solution, which is essential to get the well-ordered material.[30] The tightly capped jars were kept in an oven at 120 °C under static conditions. After 24 h, the solutions were cooled to room temperature and the precipitates were isolated by centrifugation. The solids were washed with 40 mL of DMF three times and followed by washing with 40 mL of methanol three times. During each wash, the MOF suspension was kept at room temperature for 24 h before being centrifuged. The solvent was decanted. Finally, the solids were dried at 150 °C under vacuum.

Synthesis of Pt NCs Inside the Cavities of UiO-66-NH_2. The supported platinum NCs were prepared via impregnation. To prepare 1 wt % Pt@UiO-66-NH_2, 200 mg of vacuum-dried UiO-66-NH_2 was dispersed in 12 mL of water by sonication for 1 h at room temperature. An aqueous solution (2 mL) containing 4.3 mg of K_2PtCl_4 (Acros Organics) was added dropwise to the above solution under vigorous stirring. The vial containing the slurry was stirred at room temperature for 20 h. The impregnated UiO-66-NH_2 sample was washed with 16 mL of water four times by centrifugation and then dried at 120 °C for 8 h under a vacuum. The Pt loading could be adjusted by changing the ratio between the platinum precursor and the MOF during impregnation. The same method was used to impregnate Pt into UiO-66. The Pt^{2+} impregnated UiO-66 or UiO-66-NH_2 samples were reduced in a 10% H_2/Ar flow (H_2/Ar = 5/45 mL/min) at 200 °C for 1 h to obtain Pt NCs confined inside the cavities of UiO-66 and UiO-66-NH_2.

Synthesis of 1.7 nm Pt NCs Supported on the Surface of UiO-66-NH_2. 1.7 nm platinum metal NCs were synthesized using established methods from the literature[31] with a slight modification. NaOH (100 mg; EMD) and polyvinylpyrrolidone (PVP, MW ≈ 40 000, 214 mg; Sigma-Aldrich) were dissolved in 5.0 mL of ethylene glycol (Fisher Scientific), and then this solution was added to another 5 mL of ethylene glycol solution containing $H_2PtCl_6{\cdot}6H_2O$ (79 mg; Strem Chemicals, 99.9%) in a 50 mL round-bottom flask. Under N_2 atmosphere using a balloon, this combined solution was heated at 160 °C for 3 h with magnetic stirring.

To purify the Pt NCs, 27 mL of acetone was used to precipitate Pt NCs from 3 mL of original synthesis solution. After centrifugation at 6000 rpm for 10 min, the supernatant was discarded. The precipitates were redispersed in 6 mL ethanol and precipitated again by adding 24 mL hexanes. The supernatant was discarded after centrifugation at 6000 rpm for 10 min. The precipitate was further washed with ethanol and *n*-hexanes four more times to remove solvent and capping agent. The final precipitate was redispersed in 10 mL of ethanol by sonication.

To load 1.7 nm Pt NCs onto UiO-66-NH_2, an appropriate amount of UiO-66-NH_2 (90 mg) was weighed, and dispersed in 25 mL of ethanol by sonication. Then the Pt nanocluster solution was added dropwise to UiO-66-NH_2 solution under

dx.doi.org/10.1021/cs400982n | ACS Catal. 2014, 4, 1340−1348

vigorous magnetic stirring. The stirring was continued for another 30 min after the addition of Pt NCs. Excess ethanol was removed by rotary evaporation at 40 °C. The final sample was obtained after drying at 60 °C for 4 h under a vacuum.

Synthesis of 2.9 nm Pt Supported on the Surface of Silica Spheres. The sample was prepared according to our previously published procedure.[32] Briefly, monodisperse 2.9 nm Pt NPs were synthesized by reducing $H_2PtCl_6{\cdot}6H_2O$ (98.2 mg; Strem Chemicals, 99.9%) at 100 °C in methanol−water mixture solution (360 mL: 40 mL), in the presence of PVP (polyvinylpyrrolidone, MW ≈ 29 000, Sigma-Aldrich; 266 mg). Monodisperse SiO_2 spheres with an average particle size of 180 nm were synthesized by a modified Stöber method. Typically, 75 mL of ethanol, 10 mL of deionized water, and 3.15 mL of ammonium hydroxide (28%; EMD) were mixed and heated to 45 °C. 6.0 mL of tetraethyl orthosilicate (TEOS; 98%, Sigma-Aldrich) was injected into the above mixture solution. The solution was further stirred for another 2 h. Silica spheres were obtained after washing with ethanol several times. An $-NH_2$ group was grafted onto silica sphere surface, after heating the mixture solution comprising of 1.0 g of SiO_2, 200 μL of aminopropyltriethoxysilane (99%, Alfa Aesar), and 200 mL of isopropyl alcohol, to 80 °C for 2 h. After the mixture was washed with ethanol several times, the products were dispersed in ethanol. An appropriate amount of 2.9 nm Pt NPs solution was then added to the above amine-functionalized silica sphere solution under vigorous stirring. The final 2.9 nm Pt/SiO_2 sample was obtained after washing with ethanol several times and dried.

2.2. Instrumentation. The BET surface area measurements were performed with N_2 adsorption/desorption isotherms at −196 °C on a Micromeritics ASAP 2020 instrument. Before the analysis, the samples were evacuated at 150 °C until pressure reached 5 μmHg. Powder X-ray diffraction patterns of the samples were obtained by a STOE Stadi P powder diffractometer using Cu Kα radiation (40 kV, 40 mA, λ = 0.1541 nm). The transmission electron microscopy (TEM) and high-angle annular dark field scanning transmission electron microscopy (HAADF-STEM) images were recorded on a Tecnai G^2 F20 electron microscope operated at 200 kV. Energy-dispersive X-ray (EDX, Oxford INCA) spectra were collected at a 15° tilt on the same instrument. Transmission-mode Fourier transform infrared (FTIR) spectra were measured within the 4000−400 cm^{-1} wavenumber range using a Bruker IFS66V IR spectrophotometer with the KBr pellet technique. To minimize the influence of water, diffuse reflectance infrared Fourier transform spectroscopy (DRIFTS) measurements were performed using an Agilent Cary 670 FTIR equipped with a linearized MCT detector, a Harrick diffuse reflectance accessory, and a Praying Mantis high temperature reaction chamber. A pure MOF sample was packed in the sample cup, followed by a degassing process under 60 mL/min He (Matheson Tri-Gas, 99.999%) flow at 150 °C for 1 h. After the sample was cooled down to room temperature, the spectra were recorded at 1 cm^{-1} resolution within 4000−700 cm^{-1}. Kubelka−Munk correction was applied to generate the spectra for quantitative analysis. Platinum content in UiO-66 and UiO-66-NH_2 were determined using inductively coupled plasma atomic emission spectroscopy (ICP-AES, Perkin-Elmer 2100).

2.3. Catalysis. *Gas Phase Olefin Hydrogenation.* The hydrogenation of three olefin molecules of different sizes (C_2H_4, 1-hexene, 1,3-cyclooctadiene) was carried out in a fritted quartz U-tube reactor. Typically, 2.5 mg of catalyst was weighed and mixed with 250 mg of quartz sand. No detectable conversion was observed on pure quartz sand in the hydrogenation of ethylene. An electric furnace connected with a digital temperature controller was used to heat the quartz U-tube reactor above room temperature. A cooling pump was used when the reaction was carried out at temperatures below 20 °C.

Before reaction, the catalyst was reduced with flowing H_2/He (5/45 mL/min) at 200 °C for 1 hour. For the hydrogenation of ethylene, the reaction gases are composed of 77 mL/min He(99.999%, Matheson Tri-Gas), 1.2 mL/min C_2H_4(99.9%, Praxair), and 12 mL/min H_2 (99.999%, Linweld) at 1 atm. For the hydrogenation of 1-hexene, the reactant was introduced by passing He through a bubbler containing 1-hexene (98%, Alfa Aesar). The bubbler was flushed with He flow (10.3 mL/min) for at least 2 h before catalytic testing. The reaction gases are composed of 77 mL/min balance He, 10 mL/min He through bubbler (19 Torr 1-hexene), and 11 mL/min H_2 at 1 atm. The hydrogenation of 1,3-cyclooctadiene (COD) was carried out using the same method as 1-hexene. The reaction gases are composed of 52.2 mL/min balance He, 22.6 mL/min He through bubbler containing 1.3 Torr COD (98%, Sigma-Aldrich), and 12 mL/min H_2 at 1 atm. The reaction products were monitored by a HP 5890 gas chromatograph equipped with appropriate capillary columns (C_2H_4 hydrogenation: HP PLOT Q, 30 m × 0.25 mm × 0.25 μm; 1-hexene and COD hydrogenation: DB-1, 30 m × 0.32 mm × 0.25 μm) and a flame ionization detector. The catalytic activity was obtained when a steady state was observed.

Liquid Phase Cinnamaldehyde Hydrogenation. The hydrogenation of cinnamaldehyde was carried out in a 22 mL Parr 4740 High Pressure/High Temperature Pressure Vessel. In a typical experiment, 5 mg of reduced catalyst was added into a glass liner inserted in the autoclave and 10 mL of methanol was added as the solvent. Then the autoclave was sealed and flushed four times with 40 bar H_2 (99.995%). The catalyst was activated under 40 bar H_2 at 80 °C for 12 h with magnetic stirring at 800 rpm. After the solution cooled to room temperature, 1 mL of triethylamine (99%, Acros Organics), 400 μL of *trans*-cinnamaldehyde (98%, Alfa Aesar), and 20 μL of mesitylene (internal standard; 99%, Acros Organics) were added. The hydrogenation experiment was carried out under 40 bar H_2 at room temperature with magnetic stirring at 800 rpm. The products were analyzed on a HP 5890 gas chromatograph equipped with a HP-5 capillary column (30 m × 0.32 mm × 0.25 μm) with a flame ionization detector and SHIMADZU 5050A GC-MS equipped with a HP-5ms capillary column (30 m × 0.32 mm × 0.25 μm). The response factors of each component were determined with standard samples and were used to calculate the conversion and selectivity.

3. RESULTS AND DISCUSSION

3.1. Synthesis and Characterization. After loading Pt ions into UiO-66-NH_2 and UiO-66, we used ICP-AES to measure the actual Pt loading. For UiO-66, only 0.2 wt % Pt was detected, when we tried to load 1 wt % Pt on the MOF. The majority of Pt precursor was lost during the washing steps. For UiO-66-NH_2, we could achieve 0.97, 3.3, 10.7, and 14.4 wt % Pt loading (named as 0.97, 3.3, 10.7, and 14.4%Pt@UiO-66-NH_2) when we added Pt precursors containing 1.0, 5.0, 20, and 40 wt % Pt relative to the MOF. These results suggest the amine functional groups in UiO-66-NH_2 could strongly favor the loading of metal nanoparticle as reported in other

dx.doi.org/10.1021/cs400982n | ACS Catal. 2014, 4, 1340−1348

MOFs.[33−35] This observation is also similar to the synthesis and encapsulation of metal NPs/NCs inside the poly(amido amine) (PAMAM) dendrimers. In PAMAM dendrimer, the interaction between metal precursors and the internal amino groups of the dendrimer is believed to be the main reason for the loading of metal inside the dendrimer.[36−38]

The interaction of Pt precursors with the $-NH_2$ groups of UiO-66-NH_2 was further confirmed by FT-IR spectroscopy. As shown by the FT-IR spectra in Figure 1, the peaks at 1250 cm^{-1}

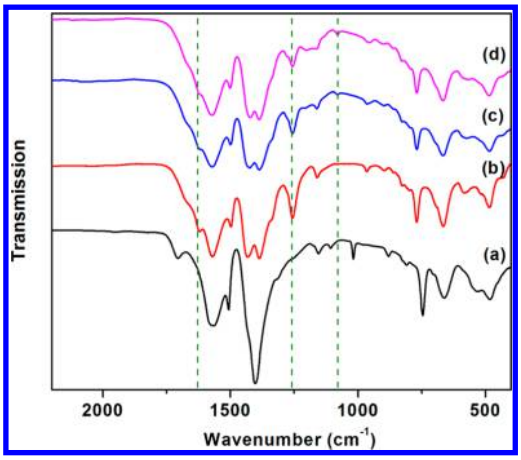

Figure 1. FT-IR spectra of (a) UiO-66, (b) UiO-66-NH_2, (c) 10.7% Pt@UiO-66-NH_2 before reduction, and (d) 14.4%Pt@UiO-66-NH_2 before reduction.

have obvious intensity changes as we increase the Pt loading in UiO-66-NH_2. Because the 1250 cm^{-1} peak does not show on the UiO-66 spectrum, it must relate to the vibration modes induced by the $-NH_2$ group. The peaks at 1250 cm^{-1} can be attributed to the C−NH_2 stretching vibrations.[39] Another two peaks at 1620 and 1080 cm^{-1} also have observable intensity changes as we increase the Pt loading. The peaks at 1620 and 1080 cm^{-1} can be attributed to the $-NH_2$ scissoring and rocking vibrations, respectively.[39] Moreover, as shown in Figure S1 (Supporting Information), the intensities of both N−H asymmetric stretching vibration peak (3521 cm^{-1}), and N−H symmetric stretching vibration peak (3405 cm^{-1}) decrease significantly with the rise in Pt loading, along with red shifts to 3518 and 3512 cm^{-1} for the former one, and 3404 and 3396 cm^{-1} for the latter one.[40] The intensity changes and position shifts of these peaks with the different loadings of K_2PtCl_4 precursor strongly suggest the interaction of $-NH_2$ groups with Pt ions. This interaction is the main reason for the easy loading of Pt ions into UiO-66-NH_2.

Electron microscopy was used to confirm that the Pt particles formed inside UiO-66-NH_2 are extremely small. Figure 2a,b shows the TEM and HAADF-STEM images of 0.97%Pt@UiO-66-NH_2, respectively. Both the TEM and HAADF-STEM images clearly show that the platinum NCs are formed inside UiO-66-NH_2 after loading K_2PtCl_4 and reducing with 10% H_2/Ar at 200 °C. To further confirm that those bright spots in the HAADF-STEM are Pt NCs, we used EDX spectroscopy to measure the elemental distribution of a selected area with and without including a bright spot (Figure S2, Supporting Information). When we selected an area with a bright spot (area 2 in Figure S2, Supporting Information), a peak at ∼9.4 keV is clearly observed, corresponding to Pt. The peak at 2.0

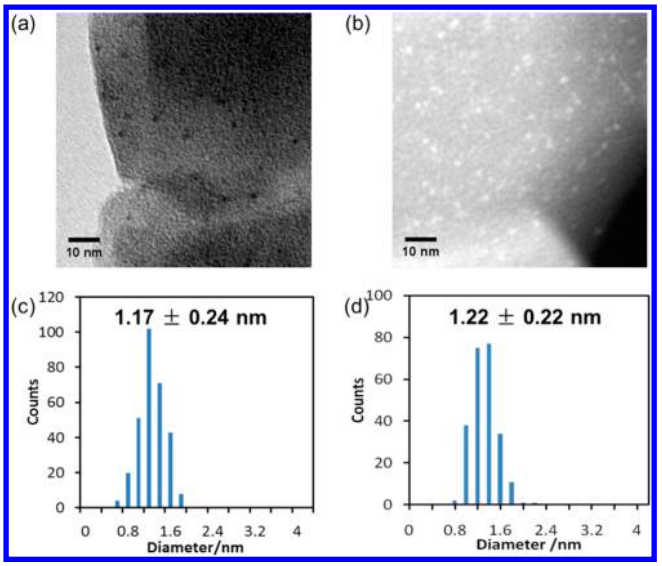

Figure 2. (a) Bright field TEM and (b) HAADF-STEM images of Pt NCs synthesized inside the cages of UiO-66-NH_2, 0.97%Pt@UiO-66-NH_2. (c) And (d) histogram of the size distribution of Pt NCs measured from the bright field TEM and the HAADF-STEM images of Pt NCs, respectively.

keV cannot be used to prove the presence of Pt because Zr from UiO-66-NH_2 also has a peak at the same position.

By measuring more than 300 Pt NCs from the TEM images, we get a mean diameter of 1.2 ± 0.2 nm. The size distribution of Pt NCs is very narrow, as shown by the histograms (Figure 2c,d) of measured NC diameters from TEM and HAADF-STEM images. Compared to previous reports on NPs/NCs supported on MOFs,[24] these TEM images showed no big particles. These TEM images and the size distribution of Pt NCs indicate that most of the Pt particles in 0.97%Pt@UiO-66-NH_2 are confined in the cages of UiO-66-NH_2 because the mean diameter of Pt particles (1.2 ± 0.2 nm) matches the diameters of the octahedral cage in UiO-66-NH_2. However, we cannot exclude the presence of smaller Pt NCs in the tetrahedral cavities of the MOF (7.5 Å) that are too small for clear observation by TEM.

More surprisingly, when we increased the Pt loading on UiO-66-NH_2 from 0.97 to 10.7 wt %, we only observed ultrasmall and monodisperse Pt NCs after reduction, as shown in Figure 3a,b. The mean diameter of these Pt NCs is 1.16 ± 0.16 nm, calculated by counting more than 300 particles. The size distribution histograms of Pt nanocluster are shown by Figure 3c,d. To the best of our knowledge, there has been no report that could achieve this high metal nanocluster loading inside MOFs and maintain a monodisperse size close to the cavity diameter of MOFs using a simple impregnation method. Additional tilting experiments were carried out to determine whether the Pt nanoclusters are located inside the MOF. As shown in Figure S3 (Supporting Information), a series of TEM pictures were taken under various tilting angles from −35° to +12°. No Pt particles were observed bulging out from the edge of the MOF during the whole tilting process, confirming that the majority of the Pt nanoclusters are located inside the MOF. We were able to track several Pt NCs during the whole tilting experiment, as indicated by the blue arrows. More interestingly, we found one big Pt particle separated into two smaller ones during the tilting experiment, as indicated by the green arrows in Figure S3 (Supporting Information), which indicated that

dx.doi.org/10.1021/cs400982n | ACS Catal. 2014, 4, 1340−1348

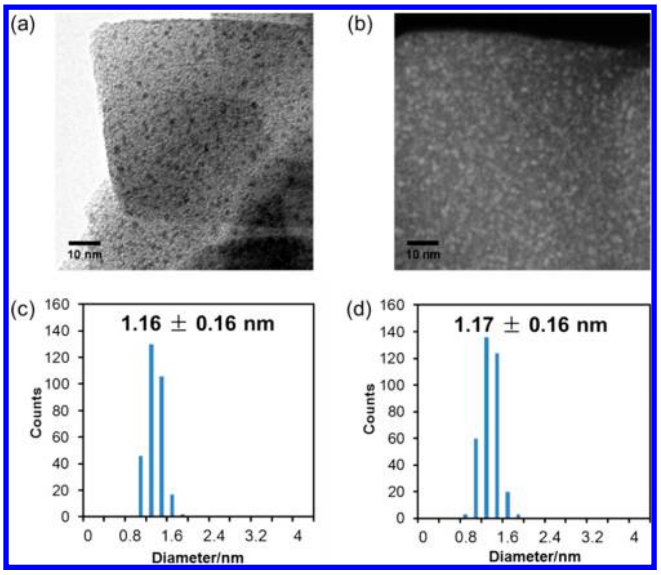

Figure 3. (a) Bright field TEM and (b) HAADF-STEM images of 10.7%Pt@UiO-66-NH_2. (c) And (d) histogram of the size distribution of Pt NCs measured from the bright field TEM and the HAADF-STEM images of Pt NCs, respectively.

some of the Pt NCs with measured diameters larger than the cavities of UiO-66-NH_2 could be caused by the overlapping of the projections of multiple small NCs in the two-dimensional TEM image.

After loading of Pt into UiO-66 and UiO-66-NH_2, we used powder X-ray diffraction (XRD) to test if the Pt loaded UiO-66 and UiO-66-NH_2 still preserved their crystal structure. The XRD patterns of the as-synthesized UiO-66 and UiO-66-NH_2 (b and c in Figure 4) matched well with the simulated XRD

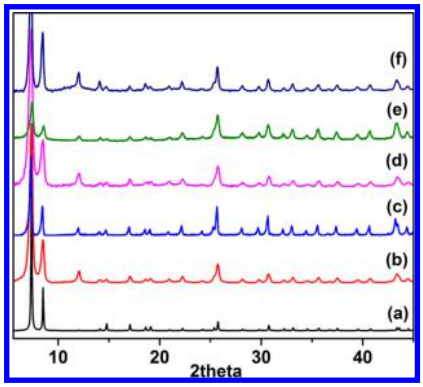

Figure 4. Powder XRD patterns of (a) simulated UiO-66, (b) as-synthesized UiO-66, (c) as-synthesized UiO-66-NH_2, (d) 0.6%Pt@UiO-66 after reduction, (e) 3.6%Pt@UiO-66-NH_2 after reduction, and (f) 10.7%Pt@UiO-66-NH_2 after reduction.

patterns (a in Figure 4). After the loading and reducing of K_2PtCl_4, there is no apparent loss of MOF crystallinity in XRD patterns (d, e, and f in Figure 4), indicating that both UiO-66 and UiO-66-NH_2 are very stable during the loading of the metal precursor in water and the reduction treatment under 10% H_2/Ar atmosphere at 200 °C for 1 h. From XRD patterns d and e in Figure 4, we did not observe any XRD peaks corresponding to fcc Pt for the reduced 0.6%Pt@UiO-66 and 3.6%Pt@UiO-66-NH_2, which indicates that the Pt particles formed after reduction are extremely small. Even for 10.7%Pt@UiO-66-NH_2 with Pt loading of 10.7 wt %, we still did not observe any diffraction peak from large Pt NPs (f in Figure 4).

It is worth pointing out that UiO-66-NH_2 is very stable under electron beam irradiation during electron microscopy measurements. The crystal structure of many MOFs, such as HKUST-1 and MIL-68(In), is easily destroyed by electron beam irradiation inside a TEM chamber.[41] With carefully reduced electron doses, Turner et al. were able to record TEM images on metal loaded MOF-5 without severe damage to its structure.[42] We found that Pt@UiO-66-NH_2 is very stable under electron beam irradiation. We did not observe any change in the size and distribution of metal NCs, as well as the morphology of UiO-66-NH_2 during our TEM measurements.

We used N_2 physisorption to measure the surface area of UiO-66-NH_2 before and after loading Pt NCs. Figure S4 (Supporting Information) shows the N_2 adsorption−desorption isotherm profiles of UiO-66-NH_2, 0.97%Pt@UiO-66-NH_2, and 10.7%Pt@UiO-66-NH_2. All adsorption−desorption isotherms show a type I shape, a characteristic of microporous materials. As shown in Table 1, The BET surface area and total

Table 1. BET Surface Area and Pore Volume of Pt loaded UiO-66 and UiO-66-NH_2 of Different Loadings

sample	BET (m^2 g^{-1})	micropore volume (cm^3 g^{-1})
UiO-66-NH_2	968	0.40
0.97%Pt@UiO-66-NH_2	782	0.30
10.7%Pt@UiO-66-NH_2	676	0.25
UiO-66	990	0.40
0.2%Pt@UiO-66	920	0.35

pore volume of UiO-66-NH_2 were calculated to be 968 m^2 g^{-1}, 0.40 cm^3 g^{-1}, respectively, which are close to the reported values.[43] Compared to UiO-66-NH_2, the BET surface area and pore volume of 0.97%Pt@UiO-66-NH_2 decreased to 782 m^2 g^{-1} and 0.30 cm^3 g^{-1}, respectively, mainly because of the occupation of the cages of UiO-66-NH_2 by Pt NCs. With 10.7 wt % loading of Pt, the BET surface area and pore volume of 10.7%Pt@UiO-66-NH_2 further drops to 676 m^2 g^{-1} and 0.25 cm^3 g^{-1}, respectively. On the contrary, the surface area of 0.2% Pt@UiO-66 only drops slightly compared to UiO-66 (from 990 to 920 m^2 g^{-1}). This small decrease in the surface area of 0.2% Pt@UiO-66 compared to UiO-66 (Figure S5, Supporting Information) is attributed to the low loading of Pt.

A temperature dependent powder XRD study on UiO-66-NH_2 reported that the MOF started losing its framework structure at 290 °C and completely decomposed at 410 °C in air.[44] To evaluate the framework stability of the Pt loaded UiO-66-NH_2 after reduction, we measured the Powder XRD patterns of 10.7%Pt@UiO-66-NH_2 with 10% H_2/Ar at different temperatures as shown in Figure 5. After reduction of 10.7% Pt@UiO-66-NH_2 at 200 °C and below for 1 h, we did not observe any change on the Powder XRD patterns. After reduction at 250 °C, most of the Powder XRD peaks are still present, but their intensity drops, which indicates that the MOF starts losing its framework structure. This temperature is lower than the 290 °C observed for UiO-66-NH_2, which suggests that 10.7%Pt@UiO-66-NH_2 has low thermal stability under a reducing environment. After reduction at 300 °C, all diffraction peaks corresponding to the UiO-66-NH_2 framework disappear, indicating complete destruction of the framework under this condition. Meanwhile, a broad diffraction peak at ∼39.5° appears, which can be attributed to the formation of small Pt

dx.doi.org/10.1021/cs400982n | ACS Catal. 2014, 4, 1340−1348

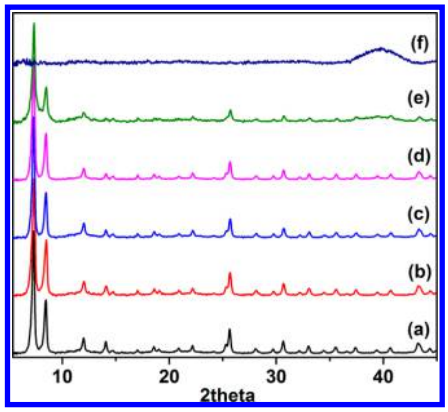

Figure 5. Powder XRD patterns of 10.7%Pt@UiO-66-NH_2 (a) before reduction, and after 1 h reduction at (b) 100 °C, (c) 150 °C, (d) 200 °C, (e) 250 °C, and (f) 300 °C.

NPs. A similar trend was also observed on 3.6%Pt@UiO-66-NH_2 (Figure S7, Supporting Information).

3.2. Hydrogenation of Ethylene, 1-Hexene, and 1,3-Cyclooctadiene. As Corma and his co-workers have pointed out, it is necessary for researchers to demonstrate the importance of having nanoparticles confined inside MOFs.[10] A prerequisite for this demonstration is to confirm that the NCs synthesized in MOFs are truly confined inside their cavities. Our tilting TEM measurements (Figure S3) strongly suggest that these Pt NCs are confined inside the cavities of UiO-66-NH_2. Here, we further prove that the Pt NCs are indeed confined inside the cavities of UiO-66-NH_2 by using 10.7%Pt@UiO-66-NH_2 as the catalyst for the hydrogenation of three model molecules (ethylene, 1-hexene and 1,3-cyclooctadiene) with different sizes. As a comparison, we also tested the catalytic activity of Pt NCs loaded on the surface of silica support.

As shown in Figure 6, Pt@UiO-66-NH_2 catalyst shows 19.6% conversion of ethylene at −30 °C. As a comparison, we prepared Pt/SiO_2 control catalyst according to our previously published procedure, which contained 2.9 nm Pt nanoparticles supported on the surface of the silica spheres.[32] An 8.5% conversion of ethylene was obtained over the control catalyst.

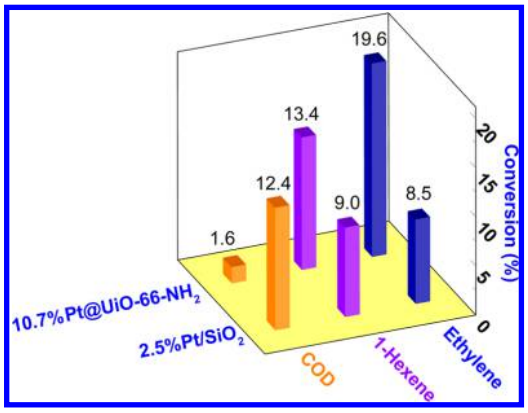

Figure 6. Comparison of 10.7%Pt@UiO-66-NH_2 (inside) and 2.5% Pt/SiO_2 in the hydrogenation of ethylene, 1-hexene and 1,3-cyclooctadiene (COD). Reaction conditions: $C_2H_4/H_2/He$ = 1.2/12/77 mL/min; 1-hexene/H_2/He = 2.5/11/87 mL/min; COD/H_2/He = 0.15/12/75 mL/min. The conversion was measured at −30 °C (ethylene), −10 °C (1-hexene), and 10 °C (COD), respectively. The same amount of Pt metal was used in the experiments.

When another linear but bigger molecule, 1-hexene, was used as the reactant, the conversion decreased to 13.4% on 10.7%Pt@UiO-66-NH_2 (corresponding to ~30% decrease). As the comparison, the conversion was maintained at 9.0% on the control catalyst. However, when 1,3-cyclooctadiene (COD) was utilized, the conversion dropped dramatically to 1.6% on 10.7%Pt@UiO-66-NH_2 but still remained at 12.4% on the control catalyst. The apparent trend of hindered conversion of bigger molecules on Pt@UiO-66-NH_2 catalysts confirms that the Pt NCs are mostly confined in the cavities of the MOF, consistent with the TEM results. It is worth noting that the activity of the Pt@UiO-66-NH_2 catalyst is almost completely inhibited in COD hydrogenation, because the size of the reactant molecule (6.7 × 6.2 × 4.2 Å) is slightly larger than the window size of UiO-66-NH_2 (ca. 6 Å).

3.3. Chemoselective Hydrogenation of Cinnamaldehyde to Cinnamyl Alcohol. The benefit of embedding Pt NCs in the MOF cavities was demonstrated by carrying out the chemoselective hydrogenation of cinnamaldehyde, as shown in Scheme 1. This reaction has been widely investigated in

Scheme 1. Hydrogenation of Cinnamaldehyde[a]

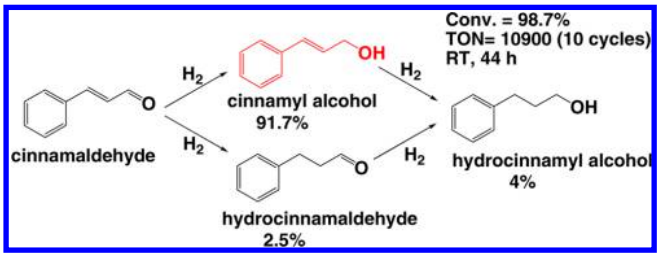

[a]Cinnamyl alcohol is the preferred product.

literature. Various heterogeneous and homogeneous catalysts, particularly noble metals including Os, Pt, Pd, Ru, Rh, Ir, and Au were found to be active for this reaction.[45−53] As shown in Scheme 1, the C═O hydrogenation product, unsaturated alcohol (cinnamyl alcohol) is industrially desired. However, low selectivity was usually observed for cinnamyl alcohol, because the C═C hydrogenation is more thermodynamically favorable than C═O hydrogenation. In particular, when carbon-supported platinum was used as the catalyst, the selectivity to cinnamyl alcohol was found to be 33%.[45] Various factors, e.g., particle size, additives, supports, and ligands, were found to dramatically influence the activity and selectivity in cinnamaldehyde hydrogenation. For example, the addition of bases could promote both the activity and the selectivity to cinnamyl alcohol.[54] Among those factors, steric effects imposed by pore/channel were proposed to enhance the selectivity in the case of Pt nanoparticle confined in microporous zeolite cavities.[55,56]

With Pt NCs confined in the cages of UiO-66-NH_2, the access of the Pt NCs is strongly restricted by the 6 Å triangular windows that connect the tetrahedral and octahedral cages inside UiO-66-NH_2. Due to the steric effect of this restriction, the C═C in the middle of a long molecule (e.g., cinnamaldehyde) cannot easily adsorb onto the surface of Pt NCs compared to the C═O at the end of the molecule. However, to the best of our knowledge, no studies have been reported on the selective hydrogenation of unsaturated aldehyde to unsaturated alcohol using the structure confinement effect of MOFs.

dx.doi.org/10.1021/cs400982n | ACS Catal. 2014, 4, 1340−1348

For the first run, a 10.7%Pt@UiO-66-NH_2 catalyst gives 85.9% conversion of cinnamaldehyde and 87.9% selectivity to cinnamyl alcohol after 42 h. The catalyst was separated by centrifugation and reused for the next run without any washing or reactivation steps. As shown in Figure 7, 10.7%Pt@UiO-66-NH_2 was used ten times without observing any sign of deactivation or decrease in cinnamyl alcohol selectivity. At the tenth run, we obtained 91.7% selectivity to cinnamyl alcohol at 98.7% conversion of cinnamaldehyde (44 h, Figure 7). A total turnover number (TON) of 10 900 was obtained after these recycling runs.

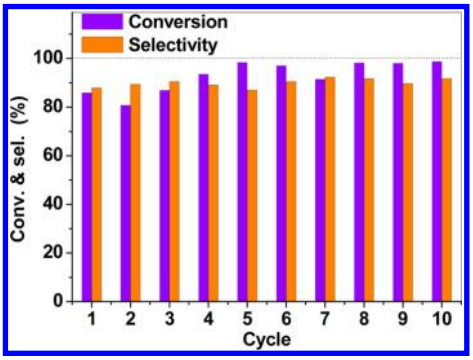

Figure 7. Recycle experiment of selective hydrogenation of cinnamaldehyde. Reaction conditions: 5.0 mg of 10.7%Pt@UiO-66-NH_2, 10 mL of methanol, 1 mL of triethylamine, 400 μL of cinnamaldehyde, 20 μL of mesitylene, 40 bar H_2, 25 °C, reaction time of 44 h (42 h for the first three runs).

We also carried out kinetic studies for the first 20 h in four recycle tests to further examine the catalyst stability.[57] As shown in Figure 8, the conversion continues to increase with reaction time, reaching ~52% after 20 h. The kinetic curves for the four recycle runs are almost overlapping with each other, which suggests the catalyst did not deactivate during these recycle runs. The selectivity to cinnamyl alcohol grows within the first 8 h, and is maintained at 90−92% afterward. Mass balance was calculated to be 96−104%, suggesting no significant reactant/products loss during recycle.

After the reaction, we conducted XRD and TEM measurements for the used catalyst. As shown in Figure S9 and S11 (Supporting Information), the respective XRD pattern and TEM images of the used catalyst do not show obvious changes compared with those of the fresh catalyst. After 10 recycle runs, some broad XRD peaks appear (Figure S9, Supporting Information), indicating a certain degree of loss in crystallinity of MOF. The surface area of the used catalysts was found to be 510 m^2/g (Figure S6, Supporting Information), slightly lower than that of the fresh reduced sample (676 m^2/g). The difference could come from residual reactants and/or products trapped in cages/channels in MOF or adsorbed on Pt metal surfaces. The microporous structure was maintained after the reaction, forming the basis for the recyclability of this catalyst.

We also performed a leaching test to examine if there are any homogeneous active species in solution that could catalyze the hydrogenation reaction. As shown in Figure S10 (Supporting Information), we did not observe any further conversion of cinnamaldehyde after we separated the solid catalyst from the reaction solution by centrifugation.

To further demonstrate the importance of the space confinement imposed by the porous structure of UiO-66-NH_2, we compared the selectivity of the MOF-confined Pt NCs with a control catalyst prepared using polyol reduction (4.2 wt % Pt/UiO-66-NH_2, outside, PVP). This control catalyst contained Pt NCs located on the external surface of the MOF, as evidenced by TEM images (Figure S12, Supporting Information). The particle size was measured to be 1.7 ± 0.2 nm, which is close to the particle size of Pt encaged in UiO-66-NH_2 (1.2 nm). Considerably lower selectivity of 71.6% at a conversion of 52.2% were observed for the control catalyst (2.0 mg of catalyst, 44 h, Table S1, Supporting Information). A commercial catalyst 5%Pt/C gave a selectivity of 71.9% with a 41.3% conversion (entry 7, Table S1, Supporting Information) at the same reaction condition. It has been well documented that bigger particles cause improved selectivity to unsaturated alcohol, due to the enhanced steric effect between bulky phenyl ring and flat Pt surface.[45,58] Considering the extremely small particle size of Pt particles confined in MOF cavities (1.2 nm), the enhanced selectivity is most likely to be caused by the steric effect imposed by the channels and/or windows of UiO-66-NH_2. The very narrow channels of MOF will force the reactant molecule to adsorb on the encaged Pt particles via the C═O group, thus hampering the adsorption of the C═C bond.[55,56] On the other hand, the pore wall, including functional ligands of the linkers, could affect the adsorption of product molecules on the Pt surface once formed. Density functional theory calculations have shown that desorption of product from Pt (111) surface is critical to control the selectivity to unsaturated alcohol in the hydrogenation of α,β-unsaturated aldehydes.[59,60]

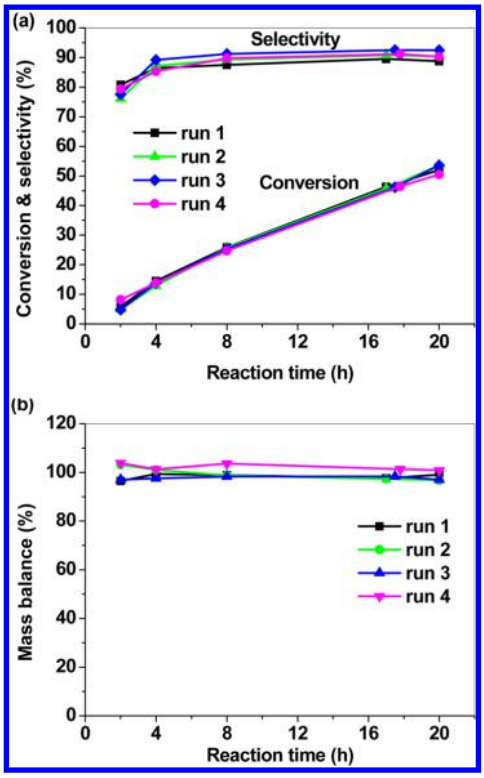

Figure 8. Kinetic studies of 10.7%Pt@UiO-66-NH_2 in cinnamaldehyde hydrogenation during recycle experiment: (a) conversion and selectivity to cinnamyl alcohol (CALC); (b) mass balance. Reaction conditions: 10 mL of methanol, 1 mL of NEt_3, 50 μL of mesitylene, 40 bar H_2, 800 rpm, rt.

4. CONCLUSIONS

We have demonstrated a simple but powerful way to achieve 10.7 wt % of monodisperse ultrasmall Pt NCs inside UiO-66-

dx.doi.org/10.1021/cs400982n | ACS Catal. 2014, 4, 1340−1348

NH_2. The size of those observed Pt NCs matches the dimension of the octahedral cavities in UiO-66-NH_2, which indicates that the cavities restrict the growth of Pt NCs and these Pt NCs are confined inside the cavities of the MOF. The confinement of Pt NCs inside the cavities of UiO-66-NH_2 was further confirmed by TEM observations under tilting, and by measuring their activity in the hydrogenation of ethylene, 1-hexene, and 1,3-cyclooctadiene. The benefit of confining Pt NCs inside the cavities of UiO-66-NH_2 is demonstrated by their more than 90% chemoselectivity to cinnamyl alcohol in the hydrogenation of cinnamaldhyde. Pt NCs supported on the external surface of the MOF give less than 72% selectivity to cinnamyl alcohol. More importantly, the MOF-confined Pt NCs are very stable under the condition used for cinnamaldehyde hydrogenation. The catalyst can be reused 10 times without any loss in activity and selectivity. We also carried out reaction kinetic studies on the MOF-confined Pt NCs in cinnamaldehyde hydrogenation and confirmed the catalyst stability during recycle runs. The stability of the MOF structure and Pt NCs are confirmed by measuring the XRD patterns and TEM images of used catalysts.

■ ASSOCIATED CONTENT

Supporting Information

DRIFT, EDX, TEM observation under tilting samples, nitrogen sorption, and PXRD measurements; kinetic studies during recycle; TEM images for the catalyst after reaction and a control sample; leaching test experimental data; catalytic results of control samples. This material is available free of charge via the Internet at http://pubs.acs.org.

■ AUTHOR INFORMATION

Corresponding Author

*W. Huang. E-mail: whuang@iastate.edu.

Author Contributions

§Z.G. and C.X. contributed equally to this work.

Notes

The authors declare no competing financial interest.

■ ACKNOWLEDGMENTS

We thank Ames Laboratory (Royalty Account) and Iowa State University for startup funds. This work was also supported by the Laboratory Research and Development Program of The Ames Laboratory. The Ames Laboratory is operated for the U.S. Department of Energy by Iowa State University under Contract No. DE-AC02-07CH11358. We thank Gordon J. Miller for use of his XRD, and Igor I. Slowing for use of his gas adsorption analyzer and ICP-AES.

■ REFERENCES

(1) Yamamoto, K.; Imaoka, T.; Chun, W. J.; Enoki, O.; Katoh, H.; Takenaga, M.; Sonoi, A. *Nat. Chem.* **2009**, *1*, 397−402.

(2) Maity, P.; Xie, S.; Yamauchi, M.; Tsukuda, T. *Nanoscale* **2012**, *4*, 4027−4037.

(3) Kaden, W. E.; Wu, T.; Kunkel, W. A.; Anderson, S. L. *Science* **2009**, *326*, 826−829.

(4) Kreno, L. E.; Leong, K.; Farha, O. K.; Allendorf, M.; Van Duyne, R. P.; Hupp, J. T. *Chem. Rev.* **2012**, *112*, 1105−1125.

(5) Li, J.-R.; Sculley, J.; Zhou, H.-C. *Chem. Rev.* **2012**, *112*, 869−932.

(6) Suh, M. P.; Park, H. J.; Prasad, T. K.; Lim, D.-W. *Chem. Rev.* **2012**, *112*, 782−835.

(7) Sumida, K.; Rogow, D. L.; Mason, J. A.; McDonald, T. M.; Bloch, E. D.; Herm, Z. R.; Bae, T.-H.; Long, J. R. *Chem. Rev.* **2012**, *112*, 724−781.

(8) Yoon, M.; Srirambalaji, R.; Kim, K. *Chem. Rev.* **2012**, *112*, 1196−1231.

(9) Cui, Y.; Yue, Y.; Qian, G.; Chen, B. *Chem. Rev.* **2012**, *112*, 1126−1162.

(10) Corma, A.; Garcia, H.; Llabres i Xamena, F. X. *Chem. Rev.* **2010**, *110*, 4606−4655.

(11) Wang, J.-L.; Wang, C.; Lin, W. *ACS Catal.* **2012**, 2630−2640.

(12) Schröder, F.; Esken, D.; Cokoja, M.; van den Berg, M. W. E.; Lebedev, O. I.; Van Tendeloo, G.; Walaszek, B.; Buntkowsky, G.; Limbach, H.-H.; Chaudret, B.; Fischer, R. A. *J. Am. Chem. Soc.* **2008**, *130*, 6119−6130.

(13) Meilikhov, M.; Yusenko, K.; Esken, D.; Turner, S.; Van Tendeloo, G.; Fischer, R. A. *Eur. J. Inorg. Chem.* **2010**, *2010*, 3701−3714.

(14) Cheon, Y. E.; Suh, M. P. *Chem.—Eur. J.* **2008**, *14*, 3961−3967.

(15) Du, D. Y.; Qin, J. S.; Wang, C. G.; Liu, X. C.; Li, S. L.; Su, Z. M.; Wang, X. L.; Lan, Y. Q.; Wang, E. B. *J. Mater. Chem.* **2012**, *22*, 21040−21044.

(16) El-Shall, M. S.; Abdelsayed, V.; Khder, A. E. R. S.; Hassan, H. M. A.; El-Kaderi, H. M.; Reich, T. E. *J. Mater. Chem.* **2009**, *19*, 7625−7631.

(17) Hermannsdörfer, J.; Friedrich, M.; Miyajima, N.; Albuquerque, R. Q.; Kümmel, S.; Kempe, R. *Angew. Chem., Int. Ed.* **2012**, *51*, 11473−11477.

(18) Houk, R. J. T.; Jacobs, B. W.; Gabaly, F. E.; Chang, N. N.; Talin, A. A.; Graham, D. D.; House, S. D.; Robertson, I. M.; Allendorf, M. D. *Nano Lett.* **2009**, *9*, 3413−3418.

(19) Li, H.; Zhu, Z.; Zhang, F.; Xie, S.; Li, H.; Li, P.; Zhou, X. *ACS Catal.* **2011**, *1*, 1604−1612.

(20) Li, P.-Z.; Aranishi, K.; Xu, Q. *Chem. Commun.* **2012**, *48*, 3173−3175.

(21) Lim, D.-W.; Yoon, J. W.; Ryu, K. Y.; Suh, M. P. *Angew. Chem., Int. Ed.* **2012**, *51*, 9814−9817.

(22) Yuan, B.; Pan, Y.; Li, Y.; Yin, B.; Jiang, H. *Angew. Chem., Int. Ed.* **2010**, *49*, 4054−4058.

(23) Zahmakiran, M. *Dalton Trans.* **2012**, *41*, 12690−12696.

(24) Esken, D.; Turner, S.; Lebedev, O. I.; Van Tendeloo, G.; Fischer, R. A. *Chem. Mater.* **2010**, *22*, 6393−6401.

(25) Aijaz, A.; Karkamkar, A.; Choi, Y. J.; Tsumori, N.; Rönnebro, E.; Autrey, T.; Shioyama, H.; Xu, Q. *J. Am. Chem. Soc.* **2012**, *134*, 13926−13929.

(26) Dhakshinamoorthy, A.; Opanasenko, M.; Cejka, J.; Garcia, H. *Catal. Sci. Technol.* **2013**, *3*, 2509−2540.

(27) Park, Y. K.; Choi, S. B.; Nam, H. J.; Jung, D.-Y.; Ahn, H. C.; Choi, K.; Furukawa, H.; Kim, J. *Chem. Commun.* **2010**, *46*, 3086−3088.

(28) Zlotea, C.; Campesi, R.; Cuevas, F.; Leroy, E.; Dibandjo, P.; Volkringer, C.; Loiseau, T.; Férey, G.; Latroche, M. *J. Am. Chem. Soc.* **2010**, *132*, 2991−2997.

(29) Cavka, J. H.; Jakobsen, S.; Olsbye, U.; Guillou, N.; Lamberti, C.; Bordiga, S.; Lillerud, K. P. *J. Am. Chem. Soc.* **2008**, *130*, 13850−13851.

(30) Schaate, A.; Roy, P.; Godt, A.; Lippke, J.; Waltz, F.; Wiebcke, M.; Behrens, P. *Chem.—Eur. J.* **2011**, *17*, 6643−6651.

(31) Wang, Y.; Ren, J.; Deng, K.; Gui, L.; Tang, Y. *Chem. Mater.* **2000**, *12*, 1622−1627.

(32) Xiao, C.; Maligal-Ganesh, R. V.; Li, T.; Qi, Z.; Guo, Z.; Brashler, K. T.; Goes, S.; Li, X.; Goh, T. W.; Winans, R. E.; Huang, W. *ChemSusChem* **2013**, *6*, 1915−1922.

(33) Huang, Y.; Zheng, Z.; Liu, T.; Lü, J.; Lin, Z.; Li, H.; Cao, R. *Catal. Commun.* **2011**, *14*, 27−31.

(34) Hwang, Y. K.; Hong, D.-Y.; Chang, J.-S.; Jhung, S. H.; Seo, Y.-K.; Kim, J.; Vimont, A.; Daturi, M.; Serre, C.; Férey, G. *Angew. Chem., Int. Ed.* **2008**, *47*, 4144−4148.

(35) Huang, Y.; Liu, S.; Lin, Z.; Li, W.; Li, X.; Cao, R. *J. Catal.* **2012**, *292*, 111−117.

(36) Crooks, R. M.; Zhao, M. Q.; Sun, L.; Chechik, V.; Yeung, L. K. *Acc. Chem. Res.* **2001**, *34*, 181−190.

(37) Scott, R. W. J.; Wilson, O. M.; Crooks, R. M. *J. Phys. Chem. B* **2005**, *109*, 692−704.
(38) Huang, W.; Kuhn, J. N.; Tsung, C.-K.; Zhang, Y.; Habas, S. E.; Yang, P.; Somorjai, G. A. *Nano Lett.* **2008**, *8*, 2027−2034.
(39) Karabacak, M.; Cinar, M.; Unal, Z.; Kurt, M. *J. Mol. Struct.* **2010**, *982*, 22−27.
(40) Peter, M.; Flores Camacho, J. M.; Adamovski, S.; Ono, L. K.; Dostert, K.-H.; O'Brien, C. P.; Roldan Cuenya, B.; Schauermann, S.; Freund, H.-J. *Angew. Chem., Int. Ed.* **2013**, *52*, 5175−5179.
(41) Houk, R. J. T.; Jacobs, B. W.; El Gabaly, F.; Chang, N. N.; Talin, A. A.; Graham, D. D.; House, S. D.; Robertson, I. M.; Allendorf, M. D. *Nano Lett.* **2009**, *9*, 3413−3418.
(42) Turner, S.; Lebedev, O. I.; Schröder, F.; Esken, D.; Fischer, R. A.; Tendeloo, G. V. *Chem. Mater.* **2008**, *20*, 5622−5627.
(43) Chavan, S.; Vitillo, J. G.; Gianolio, D.; Zavorotynska, O.; Civalleri, B.; Jakobsen, S.; Nilsen, M. H.; Valenzano, L.; Lamberti, C.; Lillerud, K. P.; Bordiga, S. *Phys. Chem. Chem. Phys.* **2012**, *14*, 1614−1626.
(44) Kandiah, M.; Nilsen, M. H.; Usseglio, S.; Jakobsen, S.; Olsbye, U.; Tilset, M.; Larabi, C.; Quadrelli, E. A.; Bonino, F.; Lillerud, K. P. *Chem. Mater.* **2010**, *22*, 6632−6640.
(45) Gallezot, P.; Richard, D. *Catal. Rev.: Sci. Eng.* **1998**, *40*, 81−126.
(46) Coq, B.; Figueras, F. *Coord. Chem. Rev.* **1998**, *178*, 1753−1783.
(47) Castillejos, E.; Debouttiere, P.-J.; Roiban, L.; Solhy, A.; Martinez, V.; Kihn, Y.; Ersen, O.; Philippot, K.; Chaudret, B.; Serp, P. *Angew. Chem., Int. Ed.* **2009**, *48*, 2529−2533.
(48) Wu, B.; Huang, H.; Yang, J.; Zheng, N.; Fu, G. *Angew. Chem., Int. Ed.* **2012**, *51*, 3440−3443.
(49) Planeix, J. M.; Coustel, N.; Coq, B.; Brotons, V.; Kumbhar, P. S.; Dutartre, R.; Geneste, P.; Bernier, P.; Ajayan, P. M. *J. Am. Chem. Soc.* **1994**, *116*, 7935−7936.
(50) Ide, M. S.; Hao, B.; Neurock, M.; Davis, R. J. *ACS Catal.* **2012**, *2*, 671−683.
(51) Bhogeswararao, S.; Srinivas, D. *J. Catal.* **2012**, *285*, 31−40.
(52) Oduro, W. O.; Cailuo, N.; Yu, K. M. K.; Yang, H.; Tsang, S. C. *Phys. Chem. Chem. Phys.* **2011**, *13*, 2590−2602.
(53) Plomp, A. J.; Vuori, H.; Krause, A. O. I.; de Jong, K. P.; Bitter, J. H. *Appl. Catal., A* **2008**, *351*, 9−15.
(54) Bhogeswararao, S.; Srinivas, D. *J. Catal.* **2012**, *285*, 31−40.
(55) Blackmond, D. G.; Oukaci, R.; Blanc, B.; Gallezot, P. *J. Catal.* **1991**, *131*, 401−411.
(56) Concepcion, P.; Perez, Y.; Hernandez-Garrido, J. C.; Fajardo, M.; Calvino, J. J.; Corma, A. *Phys. Chem. Chem. Phys.* **2013**, *15*, 12048−12055.
(57) Jones, C. *Top. Catal.* **2010**, *53*, 942−952.
(58) Galvagno, S.; Capannelli, G.; Neri, G.; Donato, A.; Pietropaolo, R. *J. Mol. Catal.* **1991**, *64*, 237−246.
(59) Loffreda, D.; Delbecq, F.; Vigné, F.; Sautet, P. *Angew. Chem., Int. Ed.* **2005**, *44*, 5279−5282.
(60) Laref, S.; Delbecq, F.; Loffreda, D. *J. Catal.* **2009**, *265*, 35−42.